# 4 Results

In this chapter, the results from the experimental will be presented.

First, doping levels were measured using XPS. Also, the quality of the produced material and the yield will be qualitatively discussed, from XPS measurements.

Then, structural observation, using SEM and STEM will be conducted. The relation of the structural observations and chemical composition, as measured in XPS will be discussed.

Finally, the spectra measured with Raman, will be analyzed. A calibration between Raman measurements, and doping measurements, from XPS, will be described, and compared to other results from the literature.

Characteristic Raman and XP spectra for each Experiment Run are displayed in the " Appendix".

## 4.1. XPS

As explained in "Methodology" chapter, in order to analyze the R-Ray spectra, it is necessary to deconvolve the element peaks observed. Figure 25 shows an example of deconvolution of the $B1s$ peak. It was measured from Boron doped SWNT produced with Triisopropyl Borate (Experiment Run 2).

The spectrum shown in Figure 25, can be well explained by four components, three of them related to oxidized forms of Boron. Among these, it can be mentioned $B_2O_3$, associated with binding energy around $193.2\ eV$ (Table 3); Magnesium-Boron-Oxygen compounds are pointed out in [35] to be around the binding energy $192.4\ eV$, and can be inferred from [70] and [71] to be possible by-products from CVD reactions in which Boron, Magnesium and Oxygen are present. Other possible oxidized forms of Boron that can be interpreted in the spectrum are the radicals $BC_2O$ and $BCO_2$, both identified in [68]: the first sits at $192\ eV$ binding energy, whereas the second appears at $190\ eV$ binding energy.

The fourth component in the $B1s$ peak is interpreted in the present work as corresponding to Boron atoms in the SWNT lattice. The component position, $191.7\ eV$, is in agreement with the range found in the literature from $191.4\ eV$ to $192.1\ eV$ (Table 3).

Owing to the bandwidth of the components, it is not always possible to distinguish some bonding environments of an element. For example, the component centered at $192.4\ eV$ in Figure 25, although identified as $Mg_2B_2O_5$, might also be interpreted to be a sum of the contributions from more than one Magnesium-Boron-Oxygen compounds, and $BCO_2$ radical, the relative amount of each cannot be determined in XPS. The same situation occurs with the Oxygen peak, which cannot be reliably deconvolved into its components. The main reason is that

Oxygen is an element with high electronegativity, thus its inner orbitals suffer minor effects from chemical bonds.

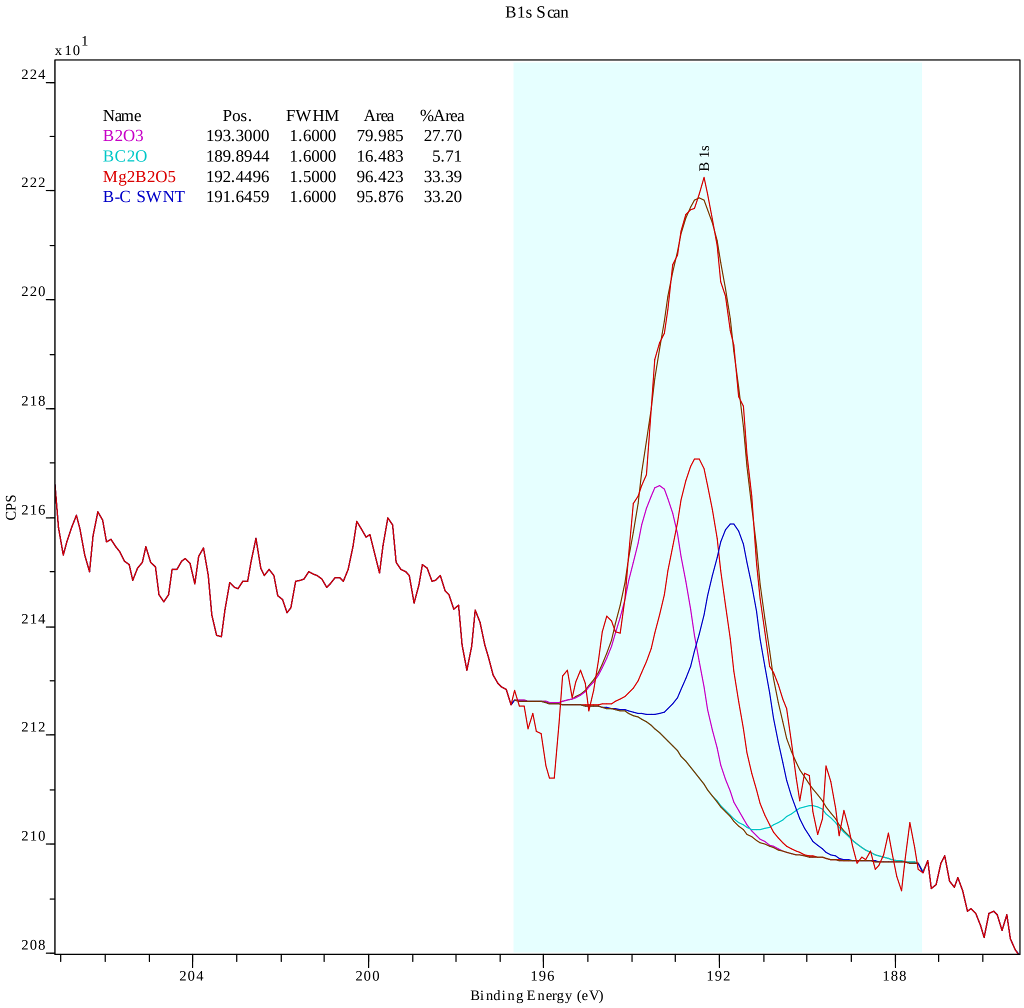

Figure 25: Spectrum B1s measured in XPS from material produced in Experiment Run 2. The peak is deconvolved in four components: $B_2O_3$, $BC_2O$/ $BCO_2$, magnesium-Boron-Oxygen compounds, and substitutional Boron in sp$^2$ Carbon Nanotube lattice. The positions, bandwidths, and areas of the components are described in the top-right inset. The light blue region in the graph highlights the peak region that was considered in the deconvolution.

The Carbon $C1s$ peak was deconvolved into the components: $C-C$, $C-O$, $C=O$, $C-B$, and $\pi-\pi^*$. Figure 26 shows $C1s$ peak of the same sample from Figure 25 (Experiment Run 2), and illustrates the deconvolution of the peak with the mentioned components.

The $C-C$ component is related to Carbon in the Nanotube lattice, although it could also be related to amorphous Carbon. As will be discussed in the next section, the Raman Spectra shows a clear SWNT signal, which is qualitative evidence that most of the $C-C$ component is indeed a contribution from Carbon in the Nanotube lattice, and the other forms of Carbon allotropes are neglected.

The $C-O$, and $C=O$ components are related to by-products, oxided forms of Carbon.

The $C-B$ component is controversial. Reference [15] interprets a component at 281.8 $eV$ as evidence of substitutional Boron within the Carbon Nanotube lattice, which is close to the position found in Figure 26 (282.3 $eV$). On the other hand, references [67,69] relate a close-by component around 282.6 $eV$ to the presence of Boron carbide material. Although not clear, the component $C-B$ seems to correspond to the shoulder observed in [15], but it is interpreted in this thesis to be related to Boron carbide, in accordance with [67,69], because this peak's area increase when Raman spectra shows weaker SWNT signal features. It is observed that this component's area is considerable when using Trimethyl Borate as precursor, which produces a worse quality material.

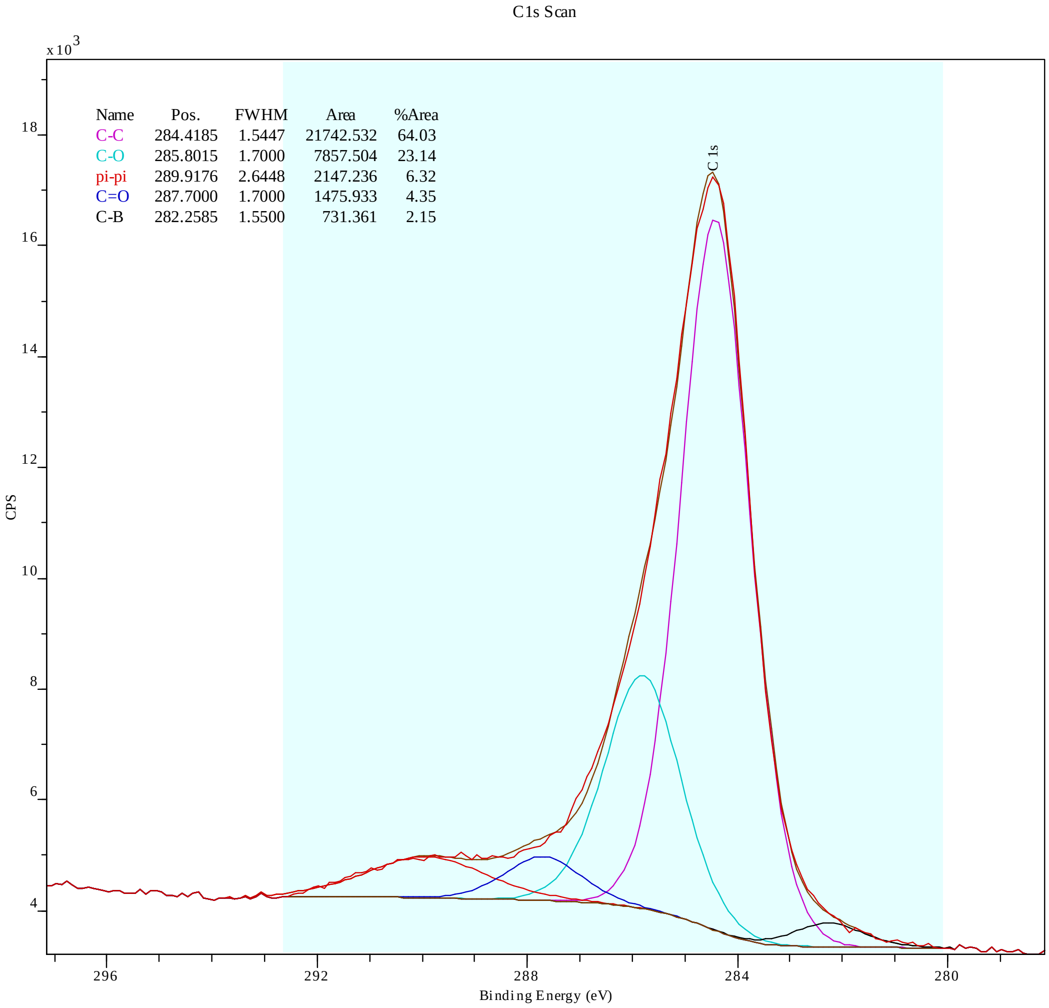

| Name | Pos. | FWHM | Area | %Area |
|---|---|---|---|---|
| C-C | 284.4185 | 1.5447 | 21742.532 | 64.03 |
| C-O | 285.8015 | 1.7000 | 7857.504 | 23.14 |
| pi-pi | 289.9176 | 2.6448 | 2147.236 | 6.32 |
| C=O | 287.7000 | 1.7000 | 1475.933 | 4.35 |
| C-B | 282.2585 | 1.5500 | 731.361 | 2.15 |

Figure 26: X-Ray Photoelectron Spectrum measurement of $C1s$ peak from the same sample of Figure 25. The upper right inset describes the components used to deconvolve the peak, with the positions, bandwidths, and areas.

To calculate the doping levels, a ratio of the areas of the $B-C$ in SWNT component in $B1s$ peak, and $C-C$ component in $C1s$ peak is calculated; but, before, each area must be divided by the corresponding peak's relative sensitivity factor (RSF). Table 5 shows the resulting doping levels calculated by this method.

The doping values found for the precursors Triisopropyl Borate, Triethyl Borate and mixtures agree with the figures found in literature, [35,61]. Reference [37] disagrees with the results of this thesis work and with the other references results. A global composition of the sample is shown in Table 6. This composition is

| | substance | Calculated doping | Controlled pressure at reactor |
|---|---|---|---|
| 1 | Ethanol | 0.00% | 65 *torr* |
| 2 | TiB | 0.89 % | 7 *torr* |
| 3 | TiB+TeB (5: 2 volume) | 1.24 % | 9 *torr* |
| 4 | TeB | 0.11 % | 13 *torr* |
| 5 | TeB | 0.84 % | 25 *torr* |
| 6 | TeB | 1.02 % | 23 *torr* |
| 7 | TmB | 15.16 % | 90 *torr* |
| 8 | TmB (@ 2 ℃) | *NO XPS* | 36 *torr* |
| 9 | TmB (@ 2 ℃) | 27.32 % | 36 *torr* |
| 10 | TmB (@ 2 ℃) | 17.58 % | 15 *torr* |
| 11 | TeB/Ethanol | *NO XPS* | 13 *torr* / 65 *torr* |
| 12 | TiB/TeB | 1.08 % | 90 *torr* / 40 *torr* |
| 13 | TiB/TeB | 0.88 % | 7 *torr* / 13 *torr* |

Table 5: this table related each precursor with its doping level, measured by the ratio of B-C component and C-C component, each normalized by its corresponding RSF factor.

| | substance | *O1s* | *C1s* | *Fe2p* | *Mg2s* | Yield Index | Controlled pressure at reactor |
|---|---|---|---|---|---|---|---|
| 1 | Ethanol | 29,3% | 49,9% | 0,6% | 20,2% | 17 | 65 *torr* |
| 2 | *TiB* | 27,9% | 49,9% | 0,8% | 20,2% | 54 | 7 *torr* |
| 3 | TiB+TeB (5: 2 volume) | 33,9% | 37,6% | 0,9% | 26,0% | 23 | 9 *torr* |
| 4 | TeB | 34,6% | 43,9% | 4,0% | 17,5% | 29 | 13 *torr* |
| 5 | TeB | 32,8% | 39,8% | 0,5% | 25,1% | 20 | 25 *torr* |
| 6 | TeB | 26,3% | 45,8% | 0,6% | 25,9% | 2 | 23 *torr* |
| 7 | TmB | 36,4% | 27,3% | 0,5% | 31,2% | 6 | 90 *torr* |
| 8 | TmB (@ 2 ℃) | 29,8% | 48,8% | 0,3% | 8,5% | 18 | 36 *torr* |
| 9 | TmB (@ 2 ℃) | 33,3% | 38,2% | 0,3% | 15,8% | 2 | 36 *torr* |
| 10 | TmB (@ 2 ℃) | 28,3% | 50,7% | 0,4% | 8,8% | 14 | 15 *torr* |
| 11 | TeB/Ethanol | − − | − − | − − | − − | − − | 13 *torr* / 65 *torr* |
| 12 | TiB/TeB | 26,4% | 54,0% | 0,9% | 17,3% | 59 | 90 *torr* / 40 *torr* |
| 13 | TiB/TeB | 22,6% | 56,6% | 1,0% | 18,8% | 46 | 7 *torr* / 13 *torr* |

Table 6: This table is a summary of the chemical composition of the samples.

found by normalizing each peak area by its RSF. The areas were measured in a Survey scan (spectrum from zero binding energy to $1100\,eV$ in coarse steps of $1\,eV$), so Boron is absent from the estimations, for it cannot be properly detected in Survey scans.

Apparently, besides the desired effect of increasing the availability of B atoms by choosing each time, smaller molecules (going from TiB to TmB), also the relative amount of available Oxygen increases. Table 6 can be used to qualitatively take some preliminary observations.

First, the “Yield Index” column is defined as the ratio of Carbon $\mathrm{C1s}$ $\mathrm{C-C}$ component’s area to Magnesium Mg1s area, and can give a rough idea of the yield of the synthesis, because the higher the amount of Carbon material deposited over the support material ($MgO$), the less is the area of support material exposed to the X-rays, taking into account that only the first few atomic layers are probed in XPS so that only the portions of the material directly shined by the X-Rays are measured. The “Yield Index” does not grasp the nature of the produced material, in the sense that, a high “yield” might mean high amount of SWNT produced, but can also reflect a higher amount of Amorphous Carbon produced. This index must be analyzed together with Raman spectra, so as to give a qualitative idea of what type of material is being produced.

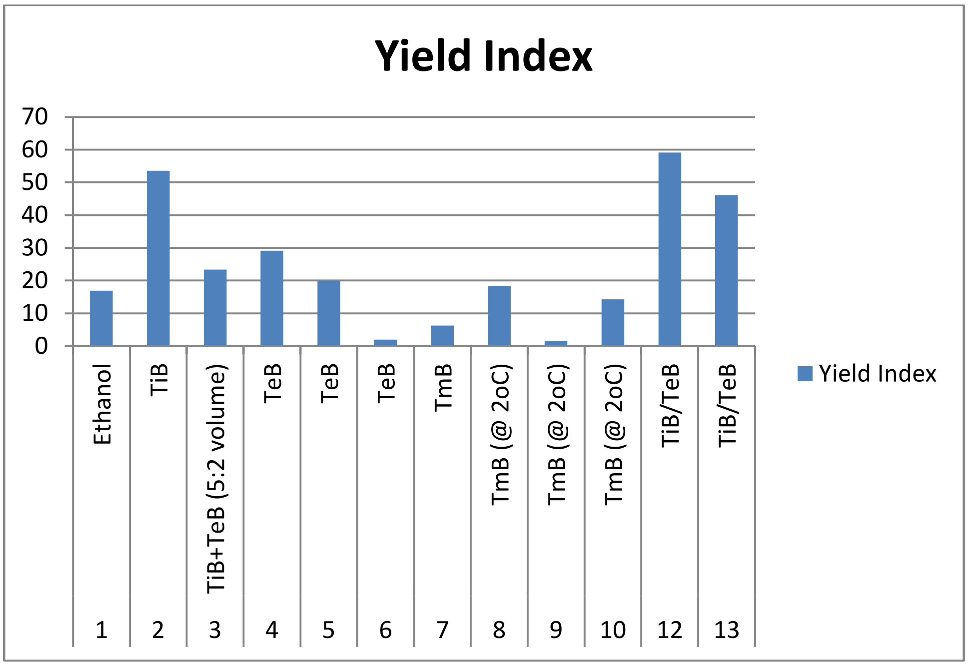

Figure 27: A graph of the “Yield Index” for the different Experiment Runs. The higher the “Yield Index” the higher should be the production yield of the sample. Experiment Run 11 is missing because no XPS measurement was done with the corresponding sample.

Figure 27 above illustrates the values of “Yield Index” presented in Table 6.

Apparently, Triisopropyl Borate is the precursor that produces Boron doped SWNT more efficiently, taking into account that the Raman shows nice SWNT spectra. This result disagrees with reference [36], which claims that Triethyl Borate is a better precursor based on a similar “Yield Index” and on SEM images. In this thesis, the three Experiment Runs using only Triethyl Borate (4, 5 and 6) resulted in worse “Yield Index”, and the SEM/STEM images show qualitatively less Carbon Nanotube material produced with this precursor. Another evidence is that the “Yield Index” obtained from mixing Triisopropyl Borate and Triethyl Borate (Experiment Run 3) is in the range of “Yield Index” obtained from Triethyl Borate alone, while the “Yield Index” obtained from using Triethyl Borate after Triisopropyl Borate is as high as from using Triisopropyl Borate alone, indicating possibly that Triethyl Borate inhibits the efficiency of the synthesis with Triisopropyl Borate. On the other hand, the discrepancies might simply be related to reproducibility issues of the synthesis method, since the present thesis and the work in [36] use the same experimental apparatus.

Also, from the graph in Figure 27, it seems that Trimethyl Borate yields the least quantity of SWNT, not only because of the small “Yield Index”, but also because the corresponding samples when measured in Raman were hard to measure as they showed low counting rates, and regions without SWNT signal. Even macroscopically, some of the samples prepared with Trimethyl Borate were composed of hard material, similar to the texture of coal.

From the above considerations, and from the graph in Figure 27, it seems that the productivity of the tested precursors decrease as the precursor molecular size decrease. A hypothesis is that as the precursor molecule’s size decreases not only the relative amount of available Boron to Carbon increases, which is the desired effect, but also the relative amount of Oxygen to Carbon increases. The higher amounts of Oxygen in the smaller precursor molecules might be etching Carbon away from the synthesis reaction, and impairing SWNT growth. The same reasoning is used in [14] to explain the production of shorter and less dense mat of Nanotubes when adding Trimethyl Borate to the Methane ($CH_4$) flow.

| | Positions | | | | |
|---|---|---|---|---|---|
| | substances | $\mathrm{B_2O_3}$ | $\mathrm{BC_2O}$ | $\mathrm{Mg-B-O}$ | $\mathrm{B-SWNT}$ |
| 1 | Ethanol | $--$ | $--$ | $--$ | $--$ |
| 2 | TiB | 193,3 | 189,9 | 192,45 | 191,65 |
| 3 | TiB+TeB (5:2 volume) | 193,29 | 189,99 | 192,23 | 191,31 |
| 4 | TeB | 193,3 | 190,13 | 192,6 | 191,20 |
| 5 | TeB | 193,5 | 189,8 | 192,2 | 191,59 |
| 6 | TeB | 193,7 | 189,82 | 192,35 | 191,50 |
| 7 | TmB | 193,5 | 190,3 | 192,52 | 191,68 |
| 8 | TmB (@ 2oC) | $--$ | $--$ | $--$ | $--$ |
| 9 | TmB (@ 2oC) | 193,92 | 190,3 | 192,6 | 191,27 |
| 10 | TmB (@ 2oC) | 194,42 | 191,00 | 193,07 | 191,92 |
| 11 | TeB/Ethanol | $--$ | $--$ | $--$ | $--$ |
| 12 | TiB/TeB | 193,4 | 190,2 | 192,47 | 191,81 |
| 13 | TiB/TeB | 193,4 | 190,14 | 192,56 | 191,61 |
| | Mean | 193,6 | 190,2 | 192,5 | 191,55 |
| | Std. Dev. | 0,3 | 0,3 | 0,2 | 0,2 |

Table 7: Mean and standard deviation values for the $B1s$ components taking into account all the Experiment Runs.

The values of the component positions measured by XPS in this thesis are in agreement with the values found in literature. Table 7 and Table 8 give the component positions for $C1s$ and $B1s$ peaks.

The component positions for the $B1s$ peak are in agreement with literature values (Table 3) within one standard deviation. Exception is the position of $B_2O_3$, which is in average upshifted in relation to literature values. It should be noted, on the other hand, that this should not influence much the calculated doping values, because the components next to the $B-C\ SWNT$ component are in the right positions.

| | Positions | | | | | |
|---|---|---|---|---|---|---|
| | substances | $\mathrm{C-C}$ | $\mathrm{C-O}$ | $\pi-\mathrm{\pi}^*$ | $\mathrm{C=O}$ | $\mathrm{C-B}$ |
| 1 | Ethanol | 284,51 | 285,21 | 288,31 | 286,51 | 282,95 |
| 2 | TiB | 284,43 | 285,85 | 289,91 | 287,70 | 282,30 |
| 3 | TiB+TeB (5:2 volume) | 284,51 | 285,88 | 289,50 | 287,34 | 282,35 |
| 4 | TeB | 284,51 | 286,17 | 288,00 | 287,50 | 282,70 |
| 5 | TeB | 284,50 | 285,97 | 288,09 | 287,35 | 282,17 |
| 6 | TeB | 284,71 | 285,82 | 287,34 | 287,05 | 282,52 |
| 7 | TmB | 284,52 | 286,08 | 290,19 | 287,90 | 282,78 |
| 8 | TmB (@ 2oC) | 284,45 | 285,84 | 288,90 | 287,50 | 293,00 |
| 9 | TmB (@ 2oC) | 284,47 | 285,73 | 286,75 | $--$ | 282,98 |
| 10 | TmB (@ 2oC) | 284,50 | 286,13 | 288,33 | 288,13 | 283,48 |
| 11 | TeB/Ethanol | $--$ | $--$ | $--$ | $--$ | $--$ |
| 12 | TiB/TeB | 284,50 | 285,87 | 287,98 | 288,00 | 282,87 |
| 13 | TiB/TeB | 284,51 | 286,07 | 290,02 | 288,07 | 282,77 |
| | Mean | 284,5 | 285,9 | 288,6 | 287,6 | 282,7 |
| | Std. Dev. | 0,1 | 0,2 | 1,1 | 0,5 | 0,3 |

Table 8: Mean and standard deviation values for the $C1s$ components taking into account all the Experiment Runs.

In Table 8, $C-C$ agrees with the position found in literature. The components related to Carbon-Oxygen Bonds $C-O$ and $C=O$ do not agree completely with literature, and it can be explained by the presence of the shake up peak $\pi \rightarrow \pi^*$ in the same energy range, which increases the uncertainty in adjusting these components. Using $Mg$ X-Ray source would solve this problem.

Component $C-B$ agrees with the values found in references [67,69], so this small shoulder in the lower binding energy region of $C1s$ peak seems to be related to the production of Boron-carbide by-production. Reference [15] claims that there exists a component at $281{,}8\,eV$ which corresponds to the substitutional Boron within Nanotube lattice; this component was not observed in the present work.

An important issue to validate the doping levels calculated in Table 5 is the possibility of there being more contribution from oxided forms of Boron than accounted for. The uncertainty of the area of the $B-C\,SWNT$ component is higher the closest is this component position to the oxided Boron components. In comparing the relative position of $B-C\,SWNT$ to the published position of $BCO_2$, one can see that the closest positions happen to the samples 7, 10 and 12. So the doping values calculated for these Experiment Runs are more uncertain, especially the very high doping levels calculated for Experiments 7 and 10.

On the other hand, the $B-C\,SWNT$ position in Experiment Run 9 is more distanced from the neighboring components, which gives more confidence on the capability of Trimethyl Borate to yield doping levels of the order of 15 %.

## 4.2. SEM+STEM

Scanning Electron Microscopy (SEM), and Scanning Transmission Electron Microscopy (STEM) was used to observe some of the produced samples. Microscopy was used to characterize morphology and to give a qualitative notion of yield. The observations from the last section will be correlated, with the following images.

The samples observed correspond to the main precursor materials: Experiment Runs 1, 2, 4 and 7.

It must be noted that SEM and STEM modes of microscopy are not used to resolve structures around $1\,nm$ size; thus, it will not be possible in general to observe an individual SWNT, except in specific conditions/acquisition parameters, and yet without a good resolution.

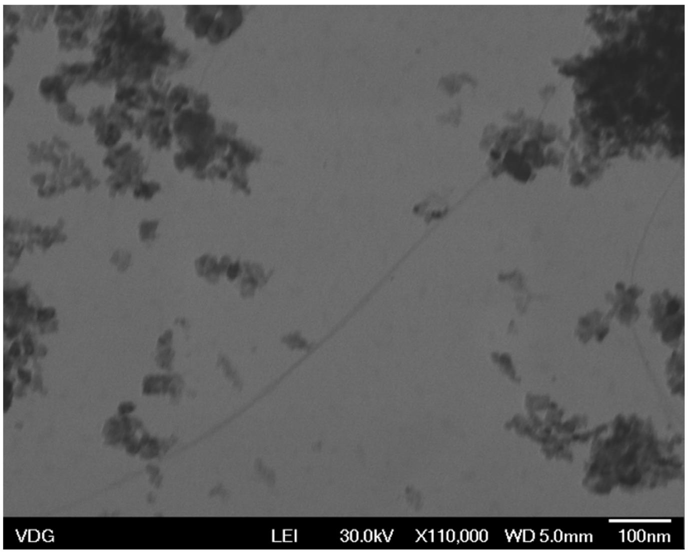

Figure 28: This image was taken in STEM mode, from sample produced in Experiment Run 1. The agglomerates of round material, can be identified as the support, $MgO$. In the center of the image, there is a tubular structure that can be a SWNT bundle or a MWNT.

Figure 28 is a typical image taken from the sample produced in Experiment Run 1, which uses Ethanol as precursor. As it can be seen from “Yield Index”, the production of this sample is low, and in the images the majority of the material is identified as the support $MgO$. In the center of the image it can be seen a tubular structure that can be identified as a bundle of SWNTs or a MWNT.

It should be noted that STEM images naturally gives the impression that less Carbon Nanotubes were produced, for the preparation of the sample for microscopy involves dispersion of the material (as explained in section " Scanning Electron Microscopy"). So, SEM and STEM images will not be compared in relation to density of Carbon Nanotubes.

In Figure 29, the sample from Experiment Run 2 is imaged in SEM mode, on the left picture, and in STEM mode, on the right picture. Experiment Run 2 uses Triisopropyl Borate as precursor. On the left side, it can be seen a high density of Carbon Nanotubes, which is in agreement with the high "Yield Index" calculated in the previous section. Also, from Raman spectra, as will be shown in next section, the Carbon Nanotubes are in truth high quality SWNT. On the right picture, some SWNTs bundles are highlighted.

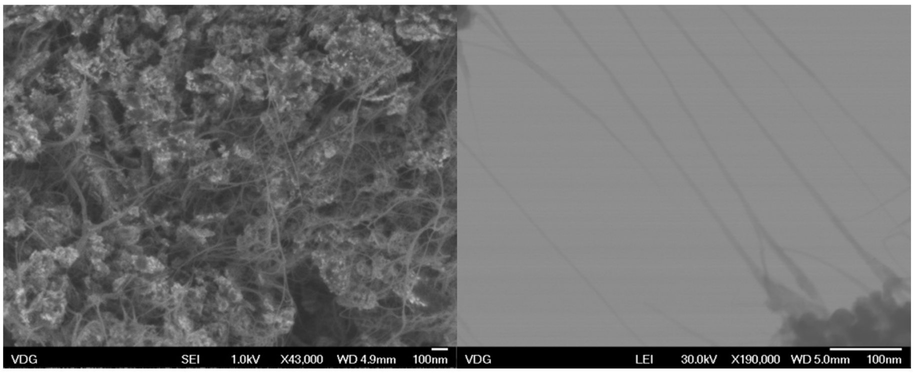

Figure 29: Images taken from sample produced in Experiment Run 2. On the left picture, SEM image shows a high density of SWNTs. On the right picture, some SWNT bundles and possibly some individual SWNTs can be seen.

Experiment Run 4 is imaged in the following figure. It evidences a yield in agreement with the "Yield Index" for Triethyl Borate: there is a low production of Carbon Nanotubes. There is the presence of some defective MWNTs, coexisting with SWNTs. This agrees with Raman spectra, as will be seen in the next section.

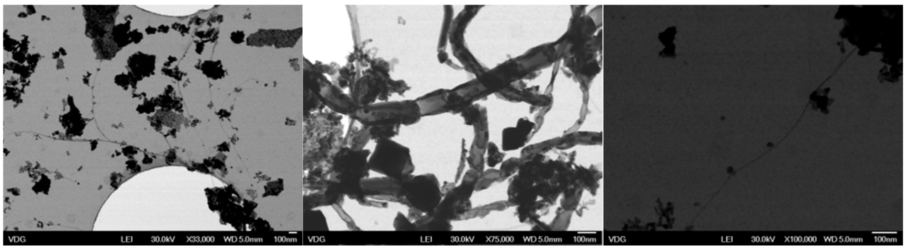

Figure 30: STEM images of Experiment Run 4 sample. On the left panel, there is a typical image of the sample. On the center panel, one can see some defective MWNTs, which will impact Raman spectra. On the right panel, there is a possibly SWNT bundle.

As a final image, Figure 31 shows Experiment Run 7 sample. In this sample, there was scarcely a Nanotube to be observed, in agreement with the low "Yield Index" for Trimethyl Borate. As will be seen in next section, there is little SWNT material, and some MWNT can be observed in the sample, right panel.

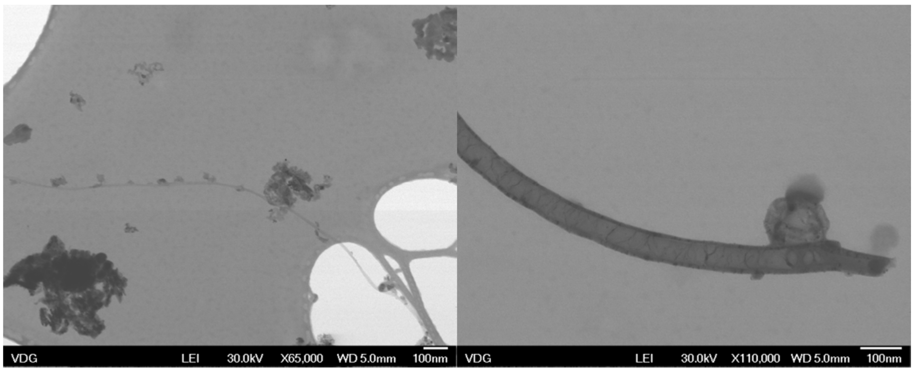

Figure 31: STEM images from sample produced in Experiment Run 7. On the left panel, there is a tubular structure, which might be a SWNT bundle or a MWNT. On the right panel, a multiwall Nanotube is imaged in detail, showing its inner compartmentalized morphology.

## 4.3. Raman

In this section, Raman spectra of the samples produced in this thesis will be discussed, in relation to the main features. Raman bands $RBM$, $D$ and $G$ will be analyzed and some conclusions will be taken in relation to the produced materials.

### 4.3.1. RBM Mode

The different Experiment Runs seem to have produced SWNTs with similar diameter distribution, for peaks at the same energy and with similar relative amplitudes have been observed.

From the RBM spectra, it is already apparent that some of the Experiment Runs did not result in SWNTs, but rather in MWNTs. Experiment Run 8, 10 and 11 are absent from Figure 32 for they produced Multiwall Carbon Nanotubes. Experiment Runs 1 and 7, produced SWNTs, but also much MWNT and amorphous by-products for it was hard to measure a typical SWNT Raman spectrum.

Qualitatively, it can be noticed that the resonances occur at the same energy positions, and that the RBM mode has roughly the same shape. From this observation, one may conclude that the same diameter distribution is to be expected for the different Experiment Runs. No further characterization was conducted, so the above affirmation remains as a hypothesis.

The main peaks identified in RBM spectra are $156.5\ cm^{-1}$, $178.5\ cm^{-1}$, and $200\ cm^{-1}$. Using formula from Figure 17 (reference [53]), one can calculate the corresponding diameters. The values are $0.65\ nm$, $0.75\ nm$ and $0.85\ nm$ respectively.

Taking into account that the wavelength used for Raman is $453\ nm$, one can calculate its energy to be $2.74\ eV$, and read this value of photon energy from Y axis in Kataura Plot in Figure 15. The calculated diameters can be read from the X axis in Kataura plot, and the pair Energy-diameter will fall in the region of near resonance of metallic single Walled Nanotubes.

Further, one might try to qualitatively assign a general structure to the Nanotubes produced in this thesis work. In Table 9, the chiralities that adjust close to the calculated diameter are painted in yellow, orange and pink. The cells formatted in boldface and underlined correspond to metallic tubes (Equation (9) in section " Electronic properties"), and are the candidate chiralities for the produced SWNTs.

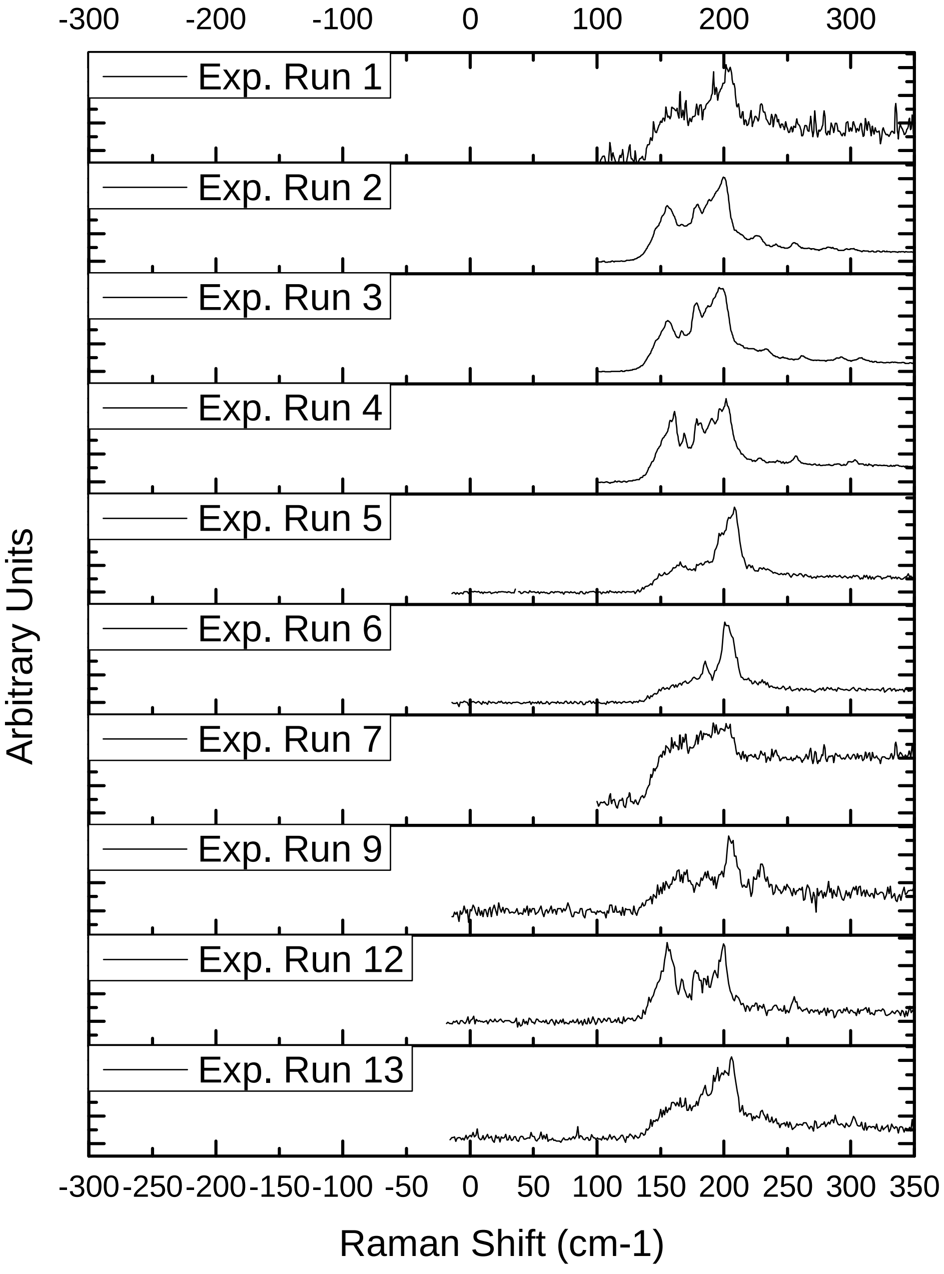

Figure 32: RBM mode for the different Experiment Runs. Each spectra represents a typical measurement for the corresponding Experiment Run. It can be noticed that some peak positions appear in more than one graph

Although the figures found in this quick analysis may not be completely correct, they serve to illustrate the concepts introduced in section " Raman Spectra of Carbon Nanotubes".

| | | n | | | | | | | | | |
|---|---|---|---|---|---|---|---|---|---|---|---|
| | | 1 | 2 | 3 | 4 | 5 | 6 | 7 | 8 | 9 | 10 |
| M | 0 | 0,08 | 0,16 | 0,23 | 0,31 | 0,39 | 0,47 | 0,55 | 0,63 | 0,70 | 0,78 |
| | 1 | 0,14 | 0,21 | 0,28 | 0,36 | 0,44 | 0,51 | 0,59 | 0,67 | 0,75 | 0,82 |
| | 2 | | 0,27 | 0,34 | 0,41 | 0,49 | 0,56 | 0,64 | **0,72** | 0,79 | 0,87 |
| | 3 | | | 0,41 | 0,48 | 0,55 | **0,62** | 0,70 | 0,77 | **0,85** | 0,92 |
| | 4 | | | | 0,54 | 0,61 | 0,68 | **0,76** | 0,83 | 0,90 | 0,98 |
| | 5 | | | | | 0,68 | 0,75 | 0,82 | 0,89 | 0,96 | 1,04 |
| | 6 | | | | | | 0,81 | 0,88 | 0,95 | 1,02 | 1,10 |
| | 7 | | | | | | | 0,95 | 1,02 | 1,09 | 1,16 |

Table 9: This table qualitatively assigns the possible chiralities associated with the Nanotubes produced in this thesis. Each pair $(n, m)$ defines a cell, which filled with the respective Nanotube diameter. The yellow, orange and pink cells correspond to the RBM resonance (or near-resonance) peaks: 156,5 $\text{cm}^{-1}$, 178,5 $\text{cm}^{-1}$, and 200 $\text{cm}^{-1}$ respectively. The boldface underlined cells correspond to the metallic tubes, which are more probably the ones in resonance with Raman laser.

Since it was observed that diameter distributions should be approximately constant throughout the Experiment Runs, curvature effects should be the same in all samples. Thus no diameter dependent shifts in peak positions should be expected, and all effect on the peak positions should be identified to doping effects. This is not strictly correct, for the diameter population was not directly probed, but the idea that doping is the dominant effect causing peak changes (in $D$, $G$, and $G'$ bands) will be used in the following sections.

## 4.3.2. D Band

The D band was used to identify structural changes in the SWNTs due to the presence of Boron within the hexagonal lattice.

The $A_D/_{A_G}$ ratio corresponds to the ratio of $D$ band and $G$ band areas, and is related to the density of defects in a Nanotube. It was calculated and related to the different precursor substances in Figure 33.

From Figure 33, it can be seen that by changing the precursor from Triisopropyl Borate, to Triethyl Borate, and then Trimethyl Borate the $A_D/_{A_G}$ ratio increases.

This agrees with the idea exposed in section " XPS", that as the precursor molecule size decrease (within these three precursors used) the amount of Oxygen available increases. The higher amount of Oxygen, not only decreases the yield of the reaction, but also increases the number of defects on the Nanotubes.

In contrast to literature, ${A_D}/{A_G}$ values are higher for the pristine SWNTs (Experiment Run 1), than for the majority of the Boron-doped SWNTs. A hypothesis is from the choice of precursor, Ethanol: the hydroxyl group of Ethanol might be etching Carbon atoms from Nanotube growth, just as Oxygen does in the other Experiment Runs. This way, the ${A_D}/{A_G}$ ratio, in this thesis is directly related to actual defects on the tubes, not the effect of the presence of an heteroatom on the hexagonal lattice.

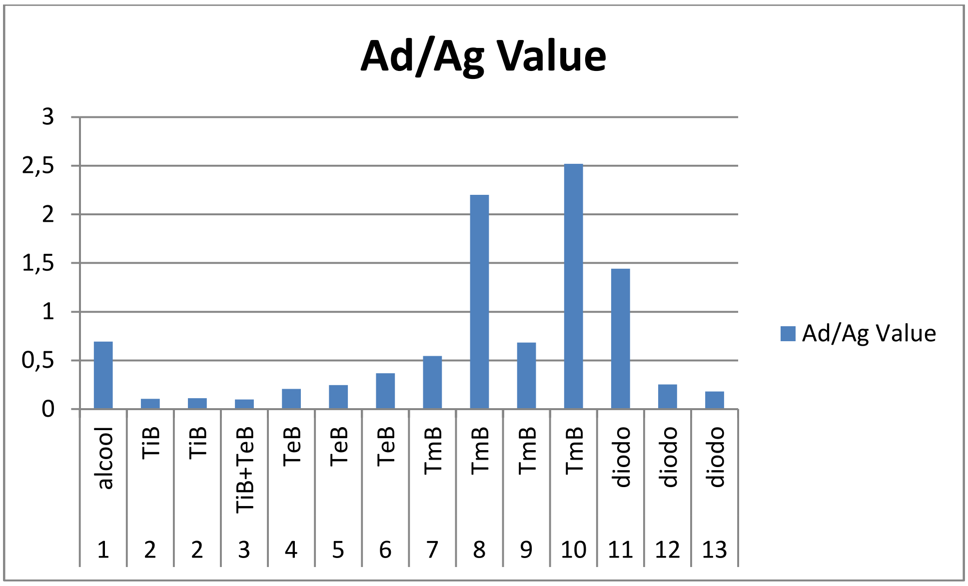

Figure 33: The graph relates different precursor substances (and different Experiment Runs) to the corresponding ${A_D}/{A_G}$ ratios. It can be noticed an increasing trend, as the precursor molecule decreases in size.

### 4.3.3. G Band

The $G$ band was investigated in order to probe for the effects of doping.

Most of the samples showed a separation of the $G$ band in $G^+$ and $G^-$ bands. This separation and the presence of a RBM band are clear evidences for the existence of SWNTs within the produced material.

The exceptions are Experiment Runs 8, 10 and 11, which also show no RBM peaks, meaning that these experiments resulted in the production of Multi Walled Carbon Nanotubes, and doped Multi Walled Nanotubes.

Experiment Run 1 was used as a reference for representing the undoped material. The $G^+$ peak position will be compared to the doped samples in order to understand the effect of doping on the Nanotubes. From section " Tangential Mode (G)", it can be seen that $G^-$ peak position is not a reliable indicator of doping, for it also depends on curvature effects.

In Figure 35, the $G^+$ peak position is depicted for the different precursor substances. It can be readily observed that the general behavior of $G^+$ position is to decrease as the precursor changes from Triisopropyl Borate, to Triethyl Borate, and then to Trimethyl Borate. This is not in agreement with literature in general, because as the molecule size decreases, the amount of Boron available to participate in Carbon Nanotube growth increases, and doping levels in SWNTs increases.

First, the increase in doping was not observed, as can be seen from Table 5 (page 61). Exception is Trimethyl Borate, which is apparently associated with high levels of doping, but even these high levels of doping are not too certain, for the reasons explained in section “ XPS”.

On the other hand, even if a trend of doping *versus* $G^+$ peak position is not clear, for there is almost no change in doping level, this peak clearly shows to be downshifted in Boron doped samples in relation to pristine samples. This result is in disagreement to the main literature results, [32,35,37,54,61].

The first hypothesis for the discrepancy is related to the uncertainties in fitting simultaneously peaks $G^-$ and $G^+$. Other vibrational modes, which were not described in the “Overview of the Research Field” chapter, might exist in the neighborhood of the $G$ band. The fact that it was not used more peaks other than $G^+$ and $G^-$ to fit data within $1400\ cm^{-1}$ and $1700\ cm^{-1}$ diminished fit quality, and increased uncertainty related to fit parameters, such as peak position. Figure 34 exemplifies the abovementioned uncertainties with a Raman spectrum taken from sample produced in Experiment Run 2.

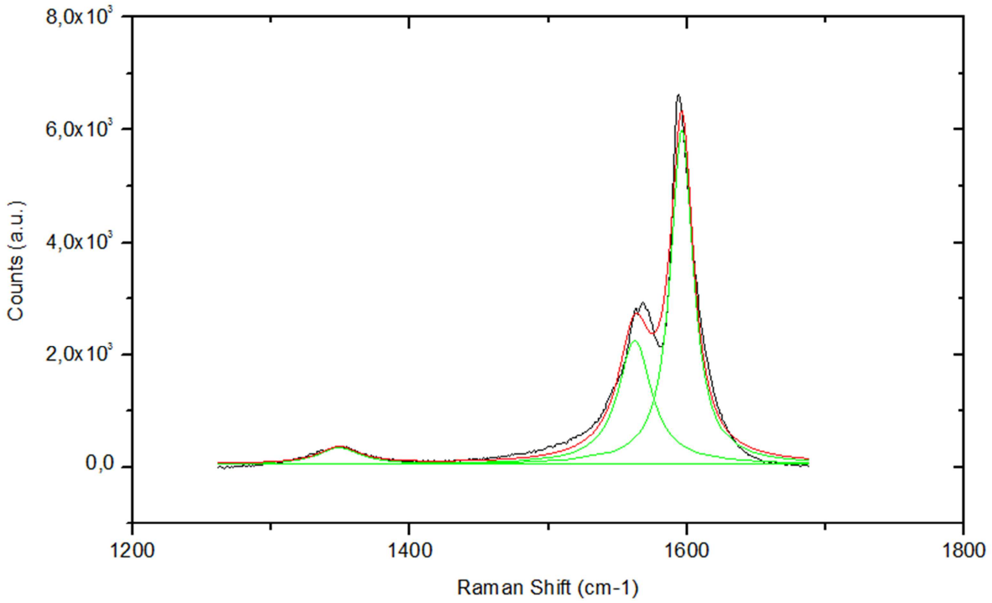

Figure 34: This graph is a Raman spectra measured around $\boldsymbol{D}$ and $\boldsymbol{G}^+$ bands of sample produced in Experiment Run 2. The black line is the measured data, while the green curves are the Lorentzians that best fit data. The red line is the sum of the green curves. It should be noted that the $\boldsymbol{G}$ band is not satisfactorily explained.

On the other hand, consistent argument can be used to support the present results. As observed in section “ RBM Mode”, the SWNTs produced are probably metallic; a laser energy of $2.0\ eV$ or $1.0\ eV$ should be used to probe the existence of semiconducting SWNTs (according to Kataura plot in Figure 15). If they are metallic indeed, then the p-doping effect of Boron would be decreased for the existence of a conductance level with zero energy gap in relation to the valence band, and with higher density of states than the acceptor level created by Boron. This way, the electrons from the valence band would "prefer" to stay at the conduction band, instead of being excited to the Boron acceptor level.

As a consequence, increasing Boron concentration would not cause a depletion of the valence band, in the case of metallic SWNTs, and the optical transition energies would be preserved. There would be in principle no shift in $G$ band. Some hole would be donated from Boron acceptor level to SWNT's valence band, indeed, as to explain the improved conductance observed in Boron doped SWNT and MWNT, in [14,16,18] for example. But the increase in Boron doping would cause less change in the optical transitions of SWNT.

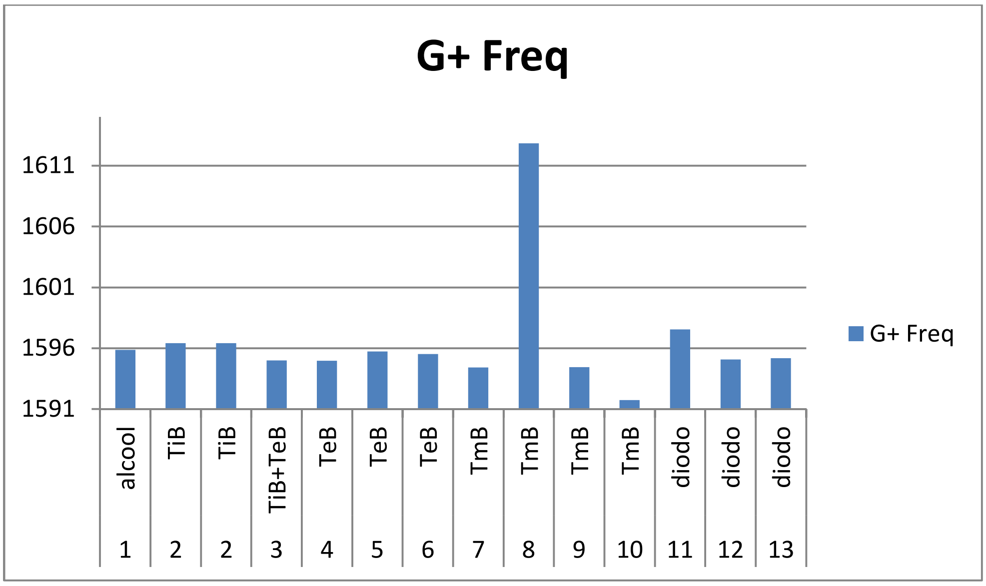

Figure 35: This graph shows the $G^+$ peak position for each Experiment Run. Except for Experiment Run 8, there is a gentle downshift in $G^+$ peak for the doped samples, in relation to the undoped one (Experiment Run 1).

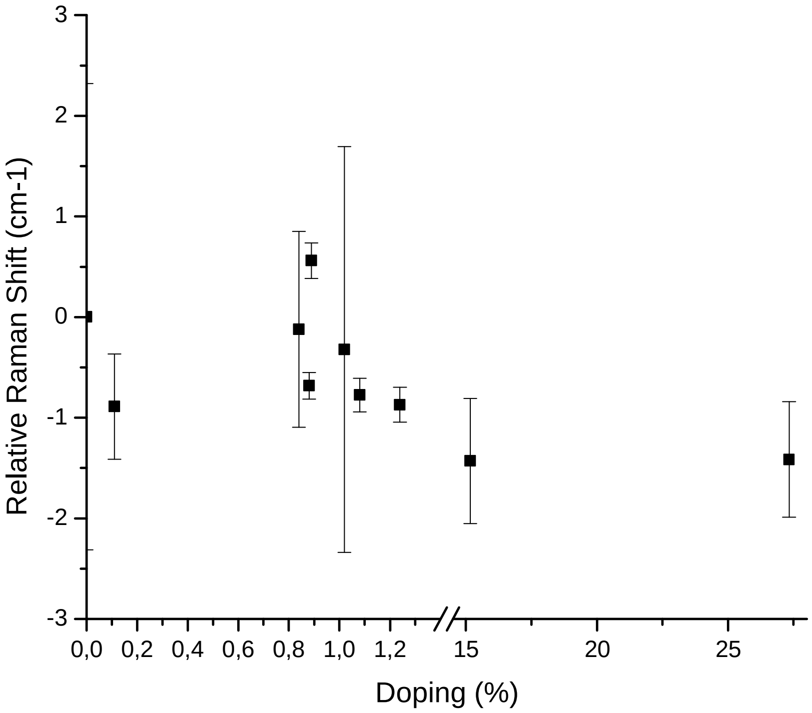

Figure 36: Plot of the relative position of $G^+$ peak of each Experiment Run in relation to the reference $G^+$ peak position, Experiment Run 1. On the horizontal axis, doping as calculated in Table 5 is plotted.

On the other hand, since $B - C$ bond is weaker than $C - C$ bond, the presence of Boron within the Nanotube's lattice would explain the gentle downshift in $G^+$ peak position, since the stronger effect from the optical transition energies is absent.

In Figure 36, a plot of relative Raman shift *versus* doping. Relative Raman shift was calculated by subtracting each Experiment Run's $G^+$ peak position by the $G^+$ peak position of Ethanol (Experiment Run 1). It can be seen the gentle downshift trend of $G^+$ peak position with increasing doping levels.